

Research papers

Investigation on thermal runaway behaviors and gas generation dynamics of lithium-ion batteries induced by electrical abuse at low-pressure conditions

Shaoyan Liu ^{a,b}, Qianzhen Guo ^b, Jiabo Zhang ^{b,c}*, Zhen Huang ^{b,c}, Dong Han ^{b,c}*

^a China-UK Low Carbon College, Shanghai Jiao Tong University, Shanghai, 200240, China

^b Key Laboratory for Power Machinery and Engineering, Ministry of Education, Shanghai Jiao Tong University, Shanghai 200240, China

^c Shanghai Non-carbon Energy Conversion and Utilization Institute, Shanghai 200240, China

ARTICLE INFO

Keywords:

Lithium-ion battery safety

Thermal runaway

Low ambient pressure

Gas generation

Electrical abuse

Kinetic parameters

ABSTRACT

With the increased demand of lithium-ion batteries in aviation and high-altitude applications, understanding battery safety at low-pressure conditions becomes paramount. This study aims to comprehensively investigate the effects of ambient pressure and charging rate on the thermal runaway behaviors and corresponding gas generation dynamics of commercial 18650-type $\text{LiNi}_{1/3}\text{Co}_{1/3}\text{Mn}_{1/3}\text{O}_2$ (NCM) cells triggered by electrical abuse, employing an accelerating rate calorimeter. The results indicate that low ambient pressure leads to an earlier opening of the safety valve and a shortened delay time of violent thermal runaway, which limits electrolyte ejection outside the cell. Due to the greater participation of electrolytes during thermal runaway, the maximum temperature and gas generation amount both increases at low ambient pressure conditions. Besides, it is found that an elevated charging rate intensifies the thermal runaway process, increasing the potential for thermal runaway hazards, as indicated by the increased generation of flammable gases. Furthermore, the Arrhenius law is employed to evaluate the gas generation dynamics of LIBs during thermal runaway by comparing the activation energy and pre-exponential factors. Therefore, the rate constants for various operation pressures and charging rates are proposed. Significantly, the rate constants show a notable increase at low-pressure conditions, highlighting the higher TR risk in such conditions.

1. Introduction

Characterized by high energy density and long cycle life, lithium-ion batteries (LIBs) have been widely adopted in electric vehicles (EVs), energy storage systems (ESSs), drones, and aircraft, spanning various operating environments including plains, plateaus and aviation sectors [1–3]. However, for LIBs, thermal runaway (TR) continues to be a significant concern in both standard and low ambient pressure environments, induced by thermal, electrical, and mechanical abuse [4]. During TR, a series of irreversible exothermic reactions gradually occur within the cell, resulting in an uncontrolled rise in temperature and potential explosion risks [5,6]. Except for the TR incidents reported at standard pressure conditions, the global number of incidents occurring at low-pressure conditions shows a continuing upward trend. According to the Federal Aviation Administration (FAA), from 2006 to 2025, over 587 aviation-related TR incidents have been reported [7]. For example, in September 2010, a United Parcel Service B747 freighter crashed in Dubai, resulting in the deaths of two pilots due to the uncontrollable LIB fires in the main cabin failed [8]. Additionally, in 2013, the failures

of LIBs in the auxiliary power unit of two Boeing 787 Dreamliners caused smoke incidents, leading to the indefinite grounding of the entire fleet [9]. Apart from aviation, high-altitude regions face similar challenges in the deployment of ESSs. These regions, with abundant renewable energy resources, are seeing widespread deployment of ESSs relying on LIBs [10]. Notable examples include a 100 MW/400 MWh ESS in Tibet, China, at 4600 m [11], a 270 MW/1080 MWh ESS in Qinghai, China, at 3000 m [12], and the world's highest ESS in Tibet, China, with 20 MW/80 MWh, at 5228 m [13]. In addition to the TR risks in ESSs, the growing adoption of EVs, drones, and aircraft in high-altitude regions increases thermal management challenges. Nearly 30% of TR incidents in such applications are attributed to heat accumulation from improper fast-charging practices [14]. This risk is further exacerbated by the low-pressure conditions of high-altitude operations.

To mitigate the risk of TR at low-pressure conditions, extensive studies have been conducted to examine TR characteristics at thermal abuse conditions. For example, Fu et al. [15] and Liu et al. [16] studied the TR behaviors of LIBs under low pressures at thermal abuse

* Corresponding authors at: Key Laboratory for Power Machinery and Engineering, Ministry of Education, Shanghai Jiao Tong University, Shanghai 200240, China.

E-mail addresses: zhangjiabo@sjtu.edu.cn (J. Zhang), dong_han@sjtu.edu.cn (D. Han).

Table 1

Summary and comparison of the thermal characteristics of LIBs at low-pressure conditions.

No.	Capacity & size	Cathode material	Trigger method	SOC	P (kPa)	T_{sc} (°C)	T_{max} (°C)	Main conclusion	Ref.
1	2.2 Ah 18,650	NCM 523	Overheating	30%	20 60 100	306 291 278	420 450 455	Low pressure influences TR by decreasing environmental cooling, triggering early venting, and lowering flame intensity.	[16]
2	2.6 Ah 18,650	LCO	Overheating	100%	30 60 90	238 228 240	475 635 713	Both ignition time and TR duration increased at low-pressure conditions, with 30 kPa identified as the critical threshold for battery ignition, below which no flame occurred.	[15]
3	2.6 Ah 18,650	LCO	Overheating	100%	64 101	125 133	824 790	The shorter ignition time of the battery during the TR process at low-pressure conditions is mainly attributed to the early opening of the safety valve.	[17]
4	2.6 Ah 18,650	NCM 523	Overheating	100%	20 60 95	133 144 159	618 643 668	Both the TR onset time and temperature decrease with lower pressure. The easier occurrence of TR at low pressures is due to the larger differential pressure, which facilitates the opening of safety valve.	[19]
5	2.6 Ah 18,650	NCM 523	Overheating	100%	30 50 70 90	111 127 136 137	502 525 592 616	The reduction of pressure delays the voltage drop, lowers TR intensity and temperature, and causes a U-shaped change in TR time due to variations in oxygen content and heat transfer efficiency, which affect ignition time and combustion behaviors.	[31]
6	5 Ah 21,700	NCM	Overheating	100%	30 50 70 90 101	232 239 237 234 230	703 745 666 768 635	LIBs are more likely to burst, and the time between safety venting and TR becomes shorter at low-pressure conditions. The rate of temperature rise during TR of LIBs depends not only on internal exothermic reactions but also on external pressure.	[32]
7	10 Ah Pouch	NCM 523	Overheating	100%	10 30 50 70 95	114 160 136 143 168	735 747 817 829 843	The combustion energy released during TR decreases due to reduced combustion efficiency, which results from the lower O ₂ mass concentration per volume at low-pressure conditions. Toxic gases like CO are more likely to be generated at low-pressure conditions.	[33]
8	2.5 Ah 18,650	NCM 111	Charging & ARC	100%	20 60 101	175 178 180	767 692 509	Low ambient pressure accelerates safety valve opening and TR onset, and leads to increased flammable gas and heat generation.	This work

conditions in a static confined space triggered by radiation-heating and hot-plate-heating methods, respectively. It was discovered that lowering atmospheric pressure significantly extended the delay time of the violent TR and weakened its intensity, which was attributed to the lower thermal decomposition reaction rates of the LIBs at low atmospheric pressure conditions. However, other studies observed a faster TR of LIBs at low-pressure conditions. Specifically, Chen et al. [17,18] and Xie et al. [19] investigated the TR and fire behaviors of LIBs with external heating and heat transfer at various ambient pressures. The results indicated that the delay time for TR decreased with the decrease of external pressure. This acceleration was attributed to the premature rupture of the safety valve at low-pressure conditions, which consequently advanced the onset of TR. From the research above, it is evident that pressure has complicated effects on TR due to the timing of the safety valve opening and the reactivity of thermal decomposition reactions, resulting in distinct TR behaviors. In addition to thermal abuse, electrical abuse is another major factor leading to TR, primarily involving external short circuits, overcharging, and over-discharging [14, 20]. Extensive research has been conducted to investigate the TR characteristics of LIBs at electrical abuse conditions under standard atmospheric pressure, including TR mechanisms [21,22], TR propagation characteristics [23,24], and TR suppression strategies [25,26]. Unlike thermal abuse, electrical abuse additionally involves electrochemical impacts, such as lithium plating, solid electrolyte interphase (SEI) film consumption, and regeneration, which affect the failure mechanisms of LIBs [27–30]. However, as summarized in Table 1, existing studies on TR at low pressures predominantly focus on thermal abuse conditions. These investigations have consistently demonstrated the influence of reduced ambient pressure on key thermal parameters such as onset temperature (T_{sc}) and maximum temperature (T_{max}). Notably, none of these works explore the interplay between low pressures and electrical abuse conditions, leaving the complex effects on TR behaviors unaddressed.

As another important characteristic of TR, understanding the gas generation mechanism is crucial for developing safer LIB designs and

mitigating TR risks [34]. To this aim, Jia et al. [35] investigated the impact of cathode materials, including LiFePO₄ (LFP), LiMn₂O₄ (LMO), and LiNi_{1/3}Co_{1/3}Mn_{1/3}O₂ (NCM), on the gas release behaviors of fully charged LIBs. It was observed that prior to the cell approaching the separator collapse temperature, the order of gas release amounts was LFP > NCM > LMO. In addition, Zhang et al. [36] investigated the gas components of LIBs with varying states of charge (SOCs) and the corresponding explosion limits. More reactive gases were found to be generated with increasing SOCs, resulting in a higher risk of TR and explosion. On the other hand, numerical models are essential for understanding and predicting TR behaviors. In the literature, thermal kinetic parameters for side reactions occurring during TR have been developed at both standard and low ambient pressure conditions [37,38]. However, these models focus only on temperature and do not consider pressure within the cell. With this objective, Mao et al. [39] examined the gas generation dynamics of 18650-type LIBs with different SOCs using an accelerating rate calorimeter (ARC). The study developed the multi-stage kinetics parameters for the gas generation process to predict the pressure within the cells, as well as the time and temperature of the rupture incident. However, kinetic parameter analyses for gas generation at low-pressure conditions still lack, which are essential for understanding the mechanism of gas generation and facilitate the early detection of TR in LIBs in the aviation and high-altitude environments.

Previous TR studies at low-pressure conditions have primarily focused on thermal abuse and heat generation behaviors. However, the combined effects of electrical abuse and low ambient pressure, along with the corresponding gas generation characteristics of LIBs, remain largely unexplored. Motivated by the research gaps mentioned above, this study aims to achieve two primary objectives: (1) to clarify the effects of ambient pressure and charging rate at low-pressure conditions on the TR behaviors triggered by electrical abuse of 18650-type NCM cells, and (2) to develop a gas generation dynamics model that incorporates kinetic parameters under various charge rates and pressures. Specifically, an ARC was employed in this study to create an

Table 2
Summary of the tested LIB characteristics.

Description (units)	Parameters
Dimensions (mm)	18 (diameter) × 65 (height)
Weight (g)	45.0 ± 0.5
Composition of electrolyte	LiPF ₆ - DEC:EMC:EC
Cathode material	LiNi _{1/3} Co _{1/3} Mn _{1/3} O ₂
Anode material	Graphite
Rated capacity (Ah)	2.56 ± 0.04
Nominal voltage (V)	3.70 ± 0.05

DEC: diethyl carbonate; EMC: ethyl methyl carbonate; EC: ethylene carbonate.

adiabatic environment, which retains the heat generated within the LIBs while eliminating external influences to explore the self-heating chain reactions of chemicals. Commercial 18650-type cells were sealed in an airtight jar within the ARC and subjected to TR tests. This allows for a more precise analysis of how pressure directly affects the thermal and chemical processes within the LIBs during TR, facilitating a better understanding of the intrinsic TR characteristics. Furthermore, the impacts of ambient pressure {1.0 atm, 0.6 atm, 0.2 atm} and charging rate {2 C, 3 C, 4 C} on the TR behaviors were systematically studied. In addition, TR gas generation dynamics models suitable for various operation pressures and charging rates have been developed.

2. Experiments

2.1. Cell samples

The sample cells used in this study were 18650-type NCM batteries (Shenzhen Doublepow Technology Co., Ltd., China), each with a diameter of 18 mm and a length of 65 mm. Note that, fresh cells are selected in this study instead of aging cells, to focus specifically on the effects of ambient pressure on TR, avoiding the potential influence caused by side reactions due to aging behaviors [40–43]. The effects of aging on TR behaviors at low-pressure conditions will be explored in future studies. To determine the exact capacity of the cells, five charge and discharge cycles using the CC-CV charging method were conducted using a battery testing system (BTS, CT-4008-5V20A-A, Shenzhen Neware Technology Co., Ltd., China). Specifically, the cells were charged at a constant rate of 0.5 C until the voltage reached the cut-off value of 4.2 V, followed by a constant voltage charging phase until the current decreased to the cut-off current of 0.04 A. After a 30 min stabilization period, the cells were discharged at a rate of 0.5 C until they reached the cut-off voltage of 2.5 V. The average capacity measured after five cycles was considered the actual capacity. The basic parameters of the cells are detailed in Table 2.

2.2. Experimental setup

The experimental setup used in this study is similar to that employed in our previous studies [36,44], with an additional vacuum pump integrated to create low-pressure conditions, as depicted in Fig. 1. Specifically, an ARC (Hangzhou YOUNG Instruction Science & Technology Co., Ltd., China) was employed to evaluate the TR behaviors of cells at various pressure conditions and charging rates. A stainless steel airtight jar with an inner radius of 39 mm and a height of 68 mm was positioned inside the ARC to establish the low-pressure condition and measure gas generation. To ensure accurate measurements during the rapid TR process [39], two N-type thermocouples were positioned on the cell. A pressure sensor with a frequency of 100 Hz was also installed. Additionally, wires soldered onto the positive and negative terminals of the cells were employed to facilitate cell charging and real-time voltage monitoring throughout the TR process. Moreover, it was validated that the margin of error in temperature and pressure measurements is approximately ±10% by multiple repetitions of experiments.

Three different ambient pressures, namely 0.2 atm, 0.6 atm, and 1.0 atm, were adopted to evaluate the characteristics of TR with a constant charging rate of 3 C. Specifically, the pressure of 0.2 atm corresponds to the typical external pressure at a cruising altitude of 10,000 m for civil aircraft [4,45], while 0.6 atm represents the ambient pressure commonly found in plateau regions [46], where ESSs are widely deployed. The standard atmospheric pressure of 1.0 atm serves as a baseline reference. Note that, for each pressure condition, the integrity of the sealing was confirmed under every pressure, and it was held stable for at least 30 min to ensure system stability. Moreover, three sets of experiments were conducted at a pressure of 0.6 atm with varying charging rates of 2 C, 3 C, and 4 C, to assess the impact of charging rate on TR at low-pressure conditions. Note that, to ensure the reliability and accuracy of the experimental data, each cell TR test was conducted at least three times at each ambient pressure and charging rate condition for cross-validation.

For each test, the initial temperature of ARC was set to 328 K (55 °C), the upper limit of the operational temperature for LIBs [47]. Once the target temperature was reached, the charging process proceeded. In this study, fresh cells at 0% SOC were used and charged using the constant current (CC) charging method to reach 100% SOC. After the self-heating process of LIBs triggered by electrical abuse, a violent TR event occurred, during which its temperature and pressure were recorded. Note that, the charging process was fully completed before TR for all cases in this study, meaning all the cells reached 100% SOC before the TR occurred. Furthermore, the composition of the produced gases was analyzed using a Gas Chromatograph (GC, Agilent 7890B). Note that, to enhance the robustness and precision of the experimental data, the cell TR tests for each condition were systematically repeated, with a minimum of three repetitions for cross-validation.

3. Results and discussion

3.1. Effects of ambient pressure

In this section, the effects of ambient pressure are investigated with a fixed charging rate of 3 C, and the ambient pressures selected for evaluation are 1.0 atm, 0.6 atm, and 0.2 atm. The evolution of cell temperature, inside-jar pressure, and voltage for these conditions is plotted in Fig. 2. Starting from 328 K (55 °C), the cell temperature continues to increase as charging begins. Even after the SOC reaches 100% and charging stops, the temperature keeps rising due to self-heating, eventually leading to a violent TR event. Two key thermal characteristic temperatures, {T_{sc}, T_{max}}, are observed to describe the TR processes. T_{sc} represents the separator collapsing temperature with temperature rise rate (dT/dt) exceeding 1 K/s [35,48,49], and T_{max} represents the maximum temperature. As observed in Fig. 2, decreasing ambient pressure from 1.0 atm to 0.2 atm significantly accelerates the occurrence of TR events, reducing τ_d from ~3300 min to ~1500 min. Furthermore, T_{sc} exhibits a monotonic decrease from 453.0 K to 448.2 K as ambient pressure decreases from 1.0 atm to 0.2 atm. Following the attainment of T_{sc}, a large amount of heat is generated within a few seconds, causing the cell to reach T_{max}, which is found to increase as ambient pressure decreases. Additionally, it is observed that the voltage change aligns closely with the temperature of the TR process. Specifically, the voltage initially drops to about 2.0 V due to the phase transition of cathode materials, followed by a period of violent fluctuation. As the internal temperature of the cell rises to T_{sc}, the separator eventually collapses, leading to a large-area internal short circuit in the cell, causing the voltage to drop to zero and indicating complete cell failure [50]. On the other hand, gas gradually accumulates within the cell as the temperature rises, causing internal pressure to increase. Note that the venting behavior highlighted in Fig. 2 results from the opening of the safety valve, which is primarily determined by the competition between the internal and ambient pressures of the cell [18]. When the internal pressure of the cell reaches a critical value, called the opening

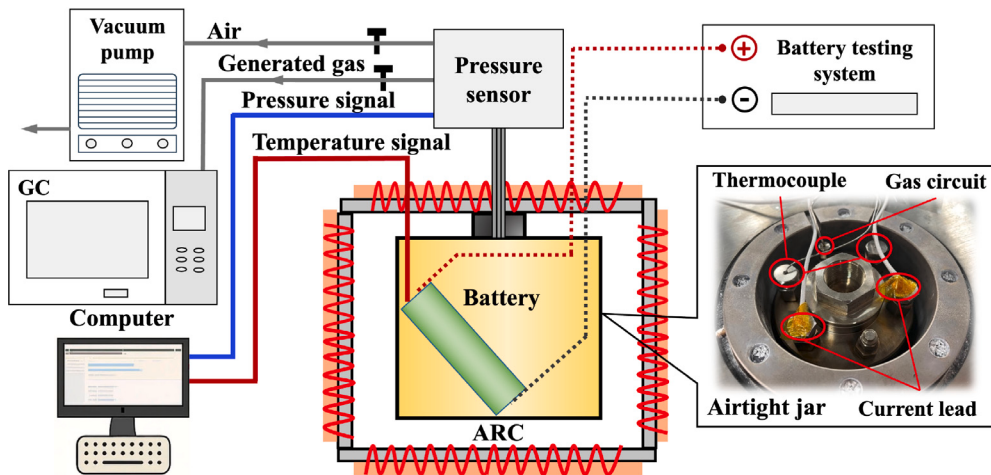


Fig. 1. Schematic of the experimental setup for temperature, current, voltage, pressure, and generated gas measurement during the TR of LIBs.

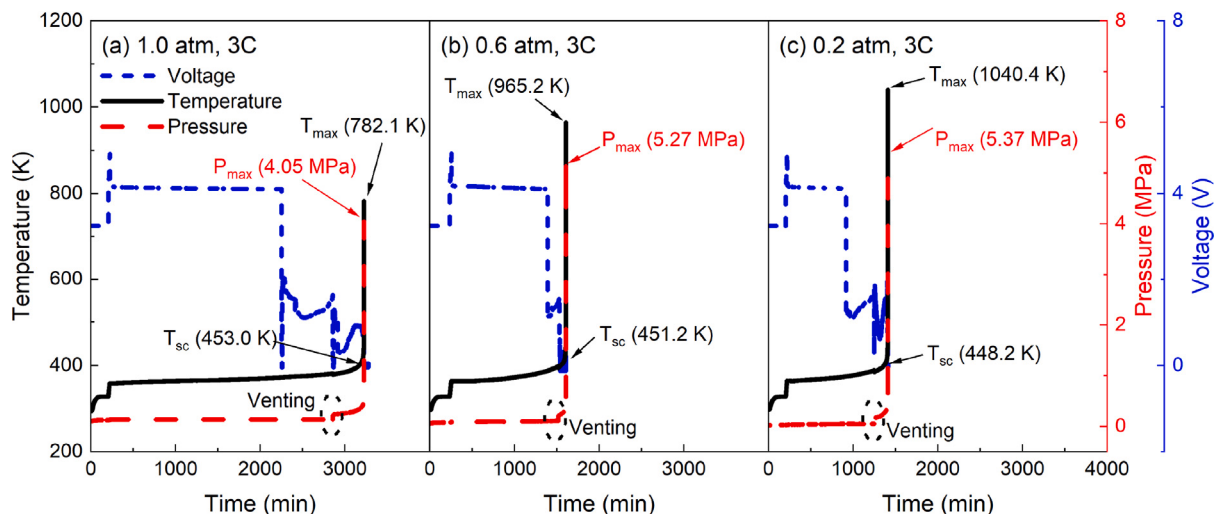


Fig. 2. Evolution of cell temperature, pressure and voltage for NCM cells at charging rate of 3 C under different pressures: (a) 1.0 atm, (b) 0.6 atm and (c) 0.2 atm.

pressure, the safety valve promptly opens. The opening pressure is defined as:

$$P_{open} = P_{valve} + P_{ambient}, \quad (1)$$

where the P_{open} is the critical internal pressure of the cell when the safety valve opens; P_{valve} is the maximum pressure difference between the interior and exterior of the cell that the safety valve can withstand, a fixed value preset during battery manufacturing; and $P_{ambient}$ is the ambient pressure.

As shown in Fig. 2, the safety valve opens earlier at low-pressure conditions. This can be explained by Eq. (1), which demonstrates that a decrease in ambient pressure ($P_{ambient}$) results in a lower opening pressure (P_{open}), causing the internal pressure of cell to reach the opening threshold more rapidly. This behavior is consistent with the findings of Refs. [16,18,19] listed in Table 1. Once the safety valve opens, the release of venting gas leads to a substantial increase in pressure outside the cell. Following T_{sc} , the pressure experiences a rapid surge, reaching its peak value, P_{max} , which increases as the ambient pressure decreases. Specifically, as the ambient pressure decreases from 1.0 atm to 0.2 atm, P_{max} consistently increases from 4.05 MPa to 5.37 MPa. Note that, the differences in P_{max} between cells with different ambient pressures are much more pronounced than those in T_{max} , indicating that the total amount of released gas varies significantly with ambient pressure.

To further analyze the impact of ambient pressure on the TR process, the temperature rise rate, dT/dt , as a function of cell temperature, is displayed for cells with different ambient pressures in Fig. 3. Three stages {Stage I, Stage II, Stage III} are defined based on different temperature rise rate characteristics. Stage I refers to the charging process during which the cell undergoes CC charging to 100% SOC. Following the completion of the charging process, in Stage II, the cell initiates self-heating caused by exothermic side reactions until the cell temperature reaches T_{sc} . After the separator collapses, the direct contact between the cathode and anode materials causes a dramatic rise in dT/dt , triggering the violent TR (Stage III). As shown in Fig. 3, a significant overlap in dT/dt under different ambient pressures is observed during Stages I and II. This is reasonable as the interior and exterior of the cell are isolated before the safety valve opens, and the self-heating process by exothermic side reactions in Stage II remains unaffected by low pressure. Note that, the enhancement of TR induced by low pressure only becomes observable in Stage III. As evidenced in Fig. 3, following T_{sc} , the maximum magnitude of dT/dt in Stage III increases as ambient pressure decreases, resulting in a higher T_{max} .

Given that battery venting gas is a critical factor leading to fire hazards and explosions, it is crucial to consider the gas generation characteristics [51–53]. The ideal gas state equation [35,39,49] can be used to calculate the amount of gas generation, denoted as n_g , as shown

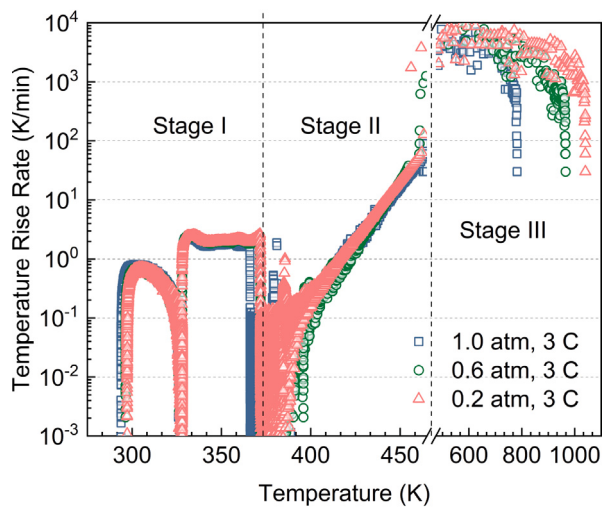


Fig. 3. The temperature rise rate, dT/dt , as a function of cell temperature for NCM cells at charging rate of 3 C under different pressures {1.0 atm, 0.6 atm, 0.2 atm}.

in Eq. (2):

$$n_g = \frac{V_a P}{Z_g R_g T} - \frac{V_a P_0}{Z_0 R_g T_0}, \quad (2)$$

where T_0 and P_0 are the initial temperature and pressure in the jar, respectively; Z_g and Z_0 are the compressible factors of the generated gases and initial gases, both of which are close to 1 [35,49,54,55]. R_g is the gas constant ($8.314 \text{ J mol}^{-1} \text{ K}^{-1}$), and V_a is the actual volume of the gas, which can be estimated using Eqs. (3) and (4) [49]:

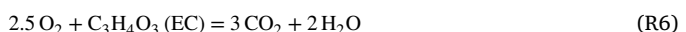
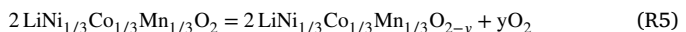
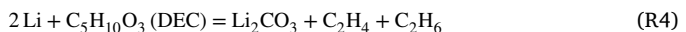
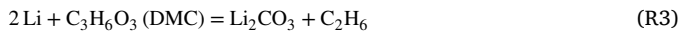
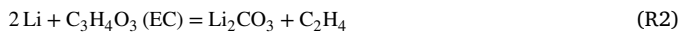
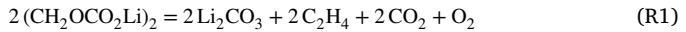
$$V_a = V_{\text{jar}} - V_{\text{cell}} + V_{\text{void}}, \quad (3)$$

$$V_{\text{void}} = 0.07 V_{\text{cell}}, \quad (4)$$

where V_{jar} is the inner volume of the jar, $3.25 \times 10^{-4} \text{ m}^3$; V_{cell} is the volume of the cell, $1.65 \times 10^{-5} \text{ m}^3$; and V_{void} is the void space within the test cell.

The gas generation amounts for cells with different ambient pressures are depicted in Fig. 4(a) and their gas compositions are plotted in Fig. 4(b). As seen in Fig. 4(a), the safety valve opens earlier at low-pressure conditions due to a lower opening pressure (P_{open}) required for activation, which results from the decrease in ambient pressure (P_{ambient}), as described by Eq. (1). Prior to the opening of the safety valve, the vapor pressure of the electrolyte is equal to the saturation pressure of the electrolyte at the vapor-liquid equilibrium [36,56]. During this period, several gas generation reactions occur. Specifically, these reactions are primarily driven by the decomposition of the SEI layer, which yields gases such as O_2 , CO_2 , and C_2H_4 [57], as depicted in R1. Following the SEI breakdown, the exposed anode further reacts with the electrolyte to generate C_2H_4 and C_2H_6 [58], as depicted in R2–R4. Meanwhile, the NCM cathode decomposes to release O_2 (R5) [59], which further promotes the gas generation reactions between the cathode and electrolyte vapors [5]. Once the safety valve opens, the concentration of organic solvent vapor outside the cell increases over time, indicating a corresponding increase in electrolyte loss within the cell [60]. Note that the electrolyte components evaporate sequentially due to their different boiling points. As the temperature rises, EMC evaporates first, followed by DEC, and finally EC [61], which then undergo the combustion reactions during Stage III, as depicted by reactions R6–R8. By comparing the gas generation in Fig. 4(a) with the heat generation in Fig. 3, it is evident that gas and heat generation respond differently to ambient pressure during Stage II. Specifically, the heat generation remains nearly unchanged under different pressures, while the gas generation shows variations, with enhanced gas generation

observed at lower ambient pressure. This difference can be explained by examining the typical gas generation reactions occurring during the TR process. At low-pressure conditions, more electrolyte remains within the cell, which enhances the electrolyte-related reaction pathways and rates of these gas generation reactions as depicted in R2–R4 and R6–R8, including its interactions with the cathode and anode materials as well as its combustion reactions [62–65]. Moreover, the maximum amount of gas generation, n_{max} , increases from 0.19 mol to 0.24 mol as the ambient pressure decreases from 1.0 atm to 0.2 atm. This increase is attributed to the reduction of electrolyte ejection outside the cell caused by the decreased τ_d at lower ambient pressure.



On the other hand, as displayed in Fig. 4(b), the amount of CO_2 within the generated gas decreases as the ambient pressure decreases from 1.0 atm to 0.2 atm, while that of CO increases. The increase in the CO/CO_2 ratio indicates a decrease in the oxidative reaction effectiveness due to the lower oxidizer density [66]. In addition, it was observed that the amount of CH_3OH decreased with lower ambient pressure, as shown in Fig. 4(b). CH_3OH is one of the primary decomposition products of dimethyl carbonate. The decline of its concentration indicates a more thorough transition to smaller molecules [67]. Consequently, the mole fractions of smaller molecules, such as H_2 , CO, and CH_4 , increase at low-pressure conditions, which agrees with Ref. [33] listed in Table 1.

3.2. Effects of charging rate at low-pressure conditions

In this section, the effects of charging rate on TR behaviors are investigated at a low ambient pressure of 0.6 atm, with the charging rate ranging from 2 C to 4 C. The evolution of cell temperature, inside-jar pressure, and voltage is plotted in Fig. 5. It is readily observed that the increased charging rate leads to an earlier and more violent TR event. Specifically, as the charging rate increases from 2 C to 4 C, τ_d decreases from ~ 2500 min to ~ 1200 min and P_{max} increases from 4.30 MPa to 5.80 MPa. Moreover, T_{sc} decreases monotonically from 466.1 K to 449.0 K with the charging rate increasing from 2 C to 4 C, indicating overcharging may lead to an early collapse of the separator. An increase in the charging rate leads to a rise in T_{max} , suggesting that the cell exhibits higher reactivity with enhanced exothermic reactions. On the other hand, similar voltage behaviors discussed in Section 3.1 are observed. Note that, as the charging rate increases, the duration for the voltage to drop to zero decreases with τ_d .

The temperature rise rate, dT/dt , as a function of cell temperature, is illustrated for cells with different charging rates in Fig. 6. In Stage I, the magnitude of dT/dt increases with the charging rate, due to the increased irreversible heat generated during charging [44,68]. Following the completion of the charging process, in Stage II, the cell initiates self-heating caused by exothermic side reactions until the cell temperature reaches T_{sc} . The increasing dT/dt in Stage I causes the cell to enter Stage II at a higher temperature, which facilitates exothermic side reactions. This, in turn, leads to an increase in dT/dt in Stage II at high charging rate. Moreover, the maximum magnitude of dT/dt , causing by the direct contact between the cathode and anode materials, increases with increased charging rates.

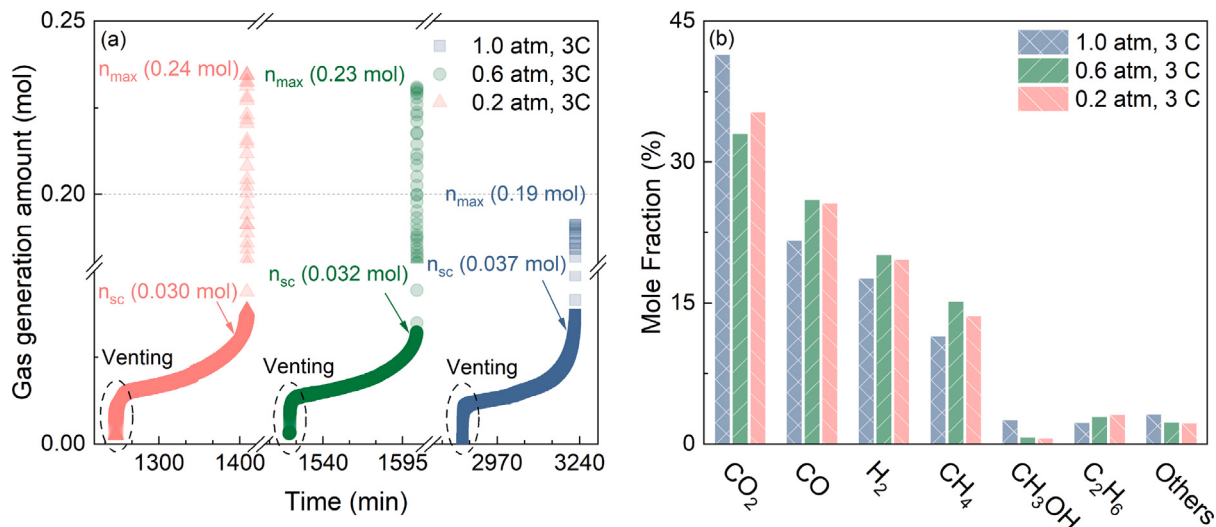


Fig. 4. The gas generation (a) amount evolution and (b) compositions for NCM cells at charging rate of 3 C under different pressures {1.0 atm, 0.6 atm, 0.2 atm}.

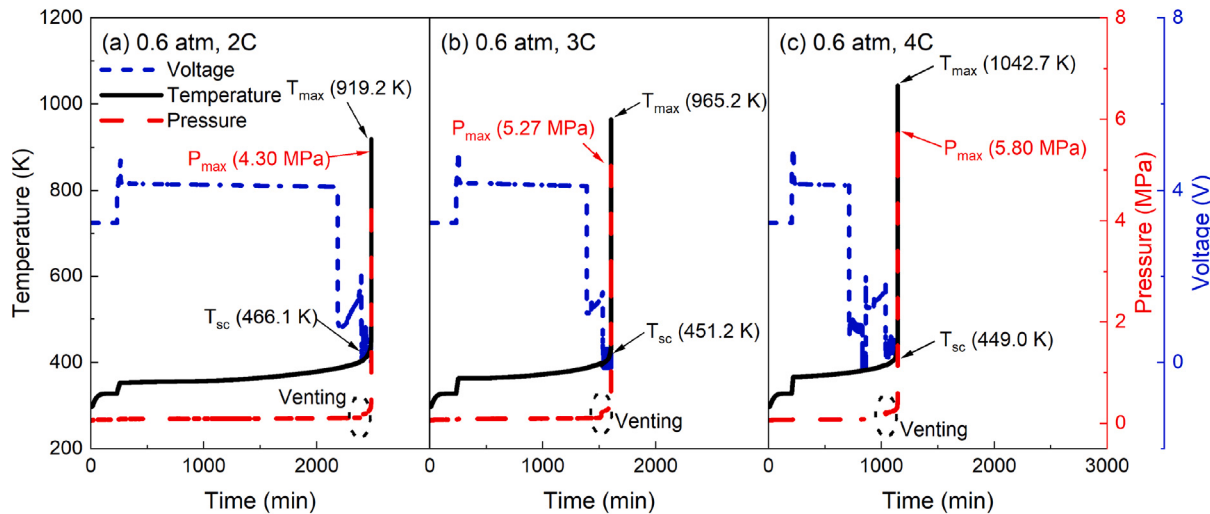


Fig. 5. Evolution of cell temperature, pressure and voltage for NCM cells under ambient pressure of 0.6 atm at different charging rates: (a) 2 C, (b) 3 C and (c) 4 C.

The gas generation amounts after the safety valve opens for cells with different charging rates are depicted in Fig. 7(a) and their gas compositions are plotted in Fig. 7(b). It is evident that, as the charging rate increases, the opening of safety valve occurs earlier, accompanied by decreases in τ_d . This is consistent with the observation that the temperature rise during Stage I increases with the charging rate and accelerates the TR process. Meanwhile, n_{sc} decreases slightly from 0.034 mol to 0.030 mol as the charging rate increases from 2 C to 4 C. This reduction in n_{sc} is due to the shortened duration of Stage II at higher charging rates as shown in Fig. 5. Note that, during Stage II, the primary gas generation reactions include the decomposition of the SEI film, breakdown of cathode/anode materials, and their interactive reactions with the electrolyte [63]. An shortened duration of Stage II enables these reactions to be less complete, thereby decreasing n_{sc} . On the other hand, the maximum amount of gas generated, n_{\max} , is observed to increase from 0.18 mol to 0.27 mol as the charging rate increases from 2 C to 4 C. The increase implies that cells with higher charging rates have an increased potential for TR hazards. Moreover, as shown in Fig. 7(b), an increase in the charging rate from 2 C to 4 C results in higher oxygen consumption and an increase in the generation of flammable gases such as CH_4 , H_2 , and CO . This phenomenon indicates that a greater extent of side reactions within the cell materials results in more flammable gases generated after TR [44,60].

3.3. Construction of gas generation dynamics models

To better understand and predict the gas generation during TR, the gas generation dynamics models suitable for various operation pressures and charging rates are developed in this section. Due to the similar physical properties of the gases generated during TR and the dominance of major gas components, it is reasonable to consider the gas product as a whole [69]. As displayed in Figs. 4(a) and 7(a), the gas generation rates in Stages II and III differ significantly. Therefore, a two-step reaction mechanism is used to describe the overall gas generation processes to represent these two stages.

As in Refs. [39], the gas generation processes of these two stages are assumed to follow the Arrhenius law. The rate of the mass consumption of reactant can be defined as Eq. (5):

$$-\frac{dm}{dt} = A \exp\left(-\frac{E_a}{R_g T}\right) m^N, \quad (5)$$

where A represents the pre-exponential factor, E_a denotes the activation energy of reaction, m is the mass of reactant, T is the temperature of reactant and N is the reaction order.

The mass of reactant can be obtained by Eq. (6):

$$m = m_0 - n \cdot \bar{M}, \quad (6)$$

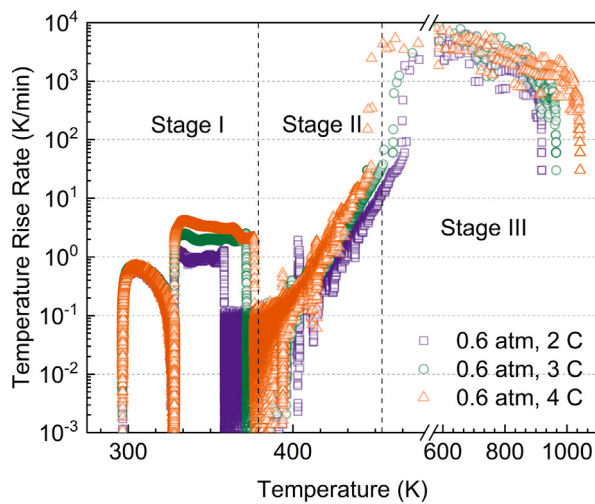


Fig. 6. The temperature rise rate, dT/dt , as a function of cell temperature for NCM cells under ambient pressure of 0.6 atm with different charging rates {2 C, 3 C, 4 C}.

where m_0 , the initial mass of the cell, is 45 g as mentioned in Table 2. \bar{M} , the molar mass, is calculated to be 28 g/mol based on the composition shown in Figs. 4(b) and 7(b) [70,71].

Substituting Eq. (6) and $N = 1$ [39,72,73] into Eq. (5):

$$\frac{dn}{dt} \cdot \bar{M} = A \exp\left(-\frac{E_a}{R_g T}\right) (m_0 - n \cdot \bar{M}), \quad (7)$$

Taking the natural logarithm of Eq. (7), then

$$\ln\left(\frac{dn}{dt}\right) + \ln \bar{M} - \ln(m_0 - n \cdot \bar{M}) = -\frac{E_a}{R_g} \cdot \frac{1}{T} + \ln A, \quad (8)$$

By plotting the curve of $\ln(dn/dt) + \ln \bar{M} - \ln(m_0 - n \cdot \bar{M})$ versus the inverse of cell temperature $1/T$, the values of E_a and A can be determined from the slope and intercept of the resulting linear fit, respectively.

Fig. 8 illustrates the curve of $\ln(dn/dt) + \ln \bar{M} - \ln(m_0 - n \cdot \bar{M})$ against the inverse of cell temperature, $1/T$, spanning from $T_{venting}$ through T_{sc} to T_{max} , considering different ambient pressures and charging rates. It can be observed that, similar to the curve of dT/dt vs. T shown in Figs. 3 and 6, the curve of $\ln(dn/dt) + \ln \bar{M} - \ln(m_0 - n \cdot \bar{M})$ vs. $1/T$ is also divided into two stages, denoted as Stage II and Stage III, by T_{sc} , suggesting distinct kinetic parameters in these two stages. The sudden increase at T_{sc} in Fig. 8 is due to the internal short circuit (ISC) caused by the interconnection between the cathode and anode materials, resulting in an instantaneous temperature rise. Consequently, a step is observed between Stage II and Stage III in Fig. 8. Note that, during the end of Stage III (~690 K to T_{max}), where the temperature and pressure rapidly increase within a few seconds, the slope becomes negative. This is because, during the TR event, the cell bursts, and the rapid ejection of hot gases occurs, leading to the non-uniformity of temperature and disrupting the synchronization between pressure and temperature [39]. Therefore, the curve near T_{max} is excluded from the subsequent kinetic parameter fitting. Additionally, it is discovered that the charging rate influences the gas generation process in both Stages II and III, while the effects of ambient pressure are primarily observed in Stage III. According to Eq. (8), the slope and intercept of the curve in Fig. 8 correspond to E_a/R_g and $\ln A$, respectively. Based on the fitting calculations of the curves, the calculated activation energy (E_a) and pre-exponential factor (A) for Stages II and III are presented in Table 3.

The rate constants for different ambient pressures and charging rates are calculated using the kinetics parameters in Table 3, and the curves of rate constants are compared in Fig. 9. Fig. 9(a) and (b) demonstrate that a high charging rate results in elevated rate

constants in both Stages II and III. This implies that increased charging rates amplify the gas generation reaction, starting from the onset at $T_{venting}$ throughout the entire TR process, highlighting the importance of regulating charging protocols. As for the effects of ambient pressure on TR gas generation, it is readily observed on Fig. 9(c) that the rate constant in Stage II remains relatively constant. Conversely, lower pressure significantly enhances the gas generation reactions in Stage III (see Fig. 9(d)). Specifically, the rate constant in Stage III increases by a factor of two as the ambient pressure decreases from 1.0 atm to 0.2 atm, highlighting the pronounced impact of ambient pressure on the kinetics during the latter stage of TR process. This indicates the potential changes in chemical reaction pathways, including reactions between the anode and cathode, the cathode and electrolyte, as well as the anode and electrolyte [62]. On the other hand, by comparing the temperature rise rates shown in Figs. 3 and 6 with the rate constants of gas generation shown in Fig. 9, it can be observed that ambient pressure exerts a stronger effect on heat generation kinetics than on gas generation kinetics during Stage III. Specifically, the heat generation rate triples as the ambient pressure decreases from 1.0 atm to 0.2 atm, whereas the gas generation rate constant only doubles. This difference can be attributed to the non-linear relationship between gas generation and heat generation [44,49,74]. One major contributor to this non-linearity is the occurrence of ISCs following separator failure, where direct contact between the anode and cathode releases the electric energy stored in the cell and generates substantial heat without gas generation [75,76]. As TR progresses, these ISC reactions become dominant in Stage III, thereby intensifying heat generation independently of gas generation. Therefore, accurately developing the kinetic parameters of gas generation reactions is essential for reliably modeling the TR process.

4. Practical implications

As a final remark, the practical implications of these gas generation kinetic parameters in improving the accuracy of internal pressure prediction during TR are discussed. Current TR modeling efforts primarily focus on temperature evolution, while quantitative pressure within the cell remains limited [37,38]. Most existing pressure models are based on sets of ODEs describing decomposition rates, energy balance, and gas flow, but rarely incorporation detailed gas generation kinetics [69,77,78]. Recently, Cheng et al. [79] proposed a thermal-pressure coupling model that incorporates gas composition data and kinetic parameters fitted from ARC experiments. By this means, their model successfully captured the internal pressure rise and TR process, proving the potential of the gas generation kinetic parameters. However, most existing studies obtain these parameters at standard pressure, with no available data at low-pressure conditions to date.

The kinetic parameters obtained in this study can enhance the accuracy of internal pressure prediction during TR and extend the modeling applicability to low-pressure environments. Besides, with these kinetic parameters, the gas evolution, internal pressure, and venting behaviors during TR can be quantitatively predicted [39]. This predictive capability enables the development of early warning strategies based on in-cell gas sensors [80,81], and extends their applicability to low-pressure environments. Moreover, the gas generation rate is a critical input for the design of ventilation, smoke exhaust, and explosion prevention systems in energy applications involving LIBs [39]. Therefore, the parameters obtained in this study not only contribute to a deeper understanding of TR mechanisms, but also provide a basis for improving battery safety, including optimizing the safety valve design and providing additional mitigation strategies.

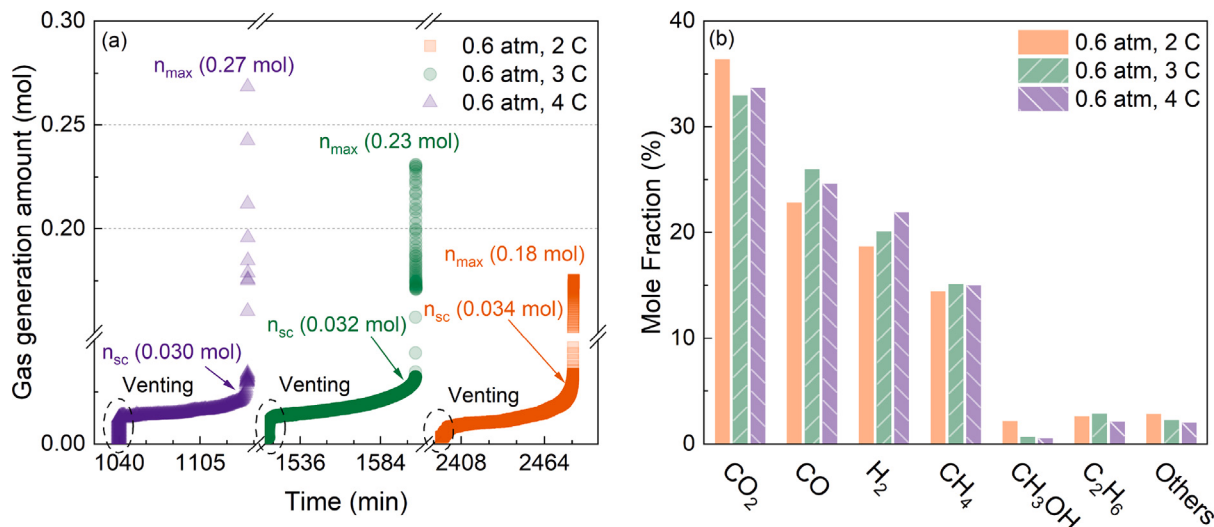


Fig. 7. The gas generation (a) amount evolution and (b) compositions for NCM cells under ambient pressure of 0.6 atm with different charging rates {2 C, 3 C, 4 C}.

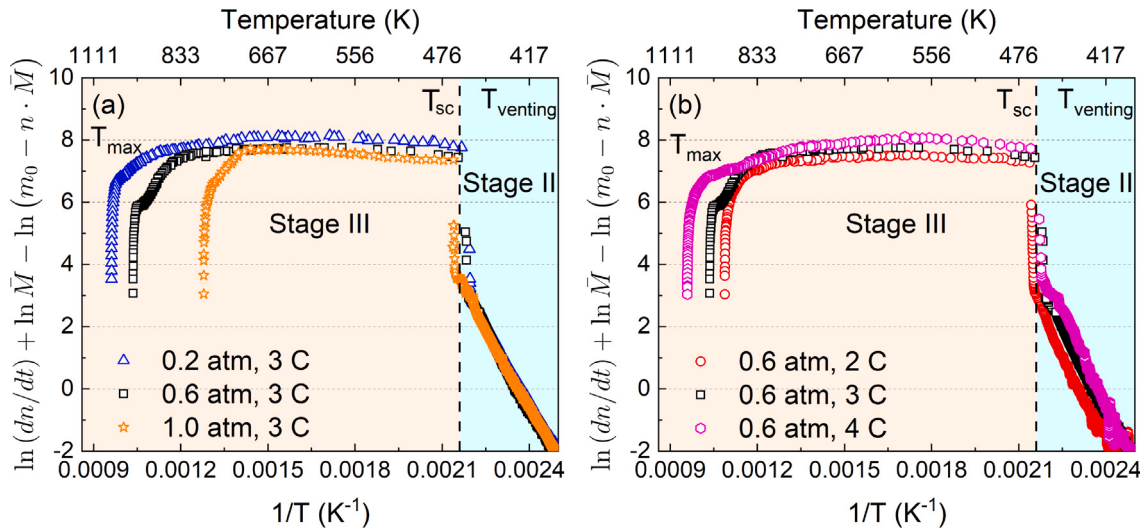


Fig. 8. Calculation of kinetics parameters of gas generation reactions with (a) different ambient pressures {1.0 atm, 0.6 atm, 0.2 atm} and (b) different charging rates {2 C, 3 C, 4 C}.

Table 3
Kinetics parameters of the gas generation reactions.

P, C	Stage II	Stage III					Stage III				
		\$-E_a/R_g\$ (K)	\$\ln A\$ (\$\ln s^{-1}\$)	\$R^2\$	\$E_a\$ (kJ mol\$^{-1}\$)	A (\$s^{-1}\$)	\$-E_a/R_g\$ (K)	\$\ln A\$ (\$\ln s^{-1}\$)	\$R^2\$	\$E_a\$ (kJ mol\$^{-1}\$)	A (\$s^{-1}\$)
0.2 atm, 3 C	-17198.79	40.78	0.99	143.99	5.15E17		-336.72	8.64	0.81	2.80	5664.99
0.6 atm, 2 C	-20259.08	46.66	0.99	168.43	1.83E20		-396.50	8.19	0.82	3.30	3591.73
0.6 atm, 3 C	-17751.02	41.82	0.99	147.58	1.45E18		-463.80	8.51	0.87	3.86	4943.06
0.6 atm, 4 C	-16598.82	39.81	0.98	138.00	1.95E17		-595.19	9.07	0.86	4.95	8730.69
1.0 atm, 3 C	-18180.96	42.84	0.97	151.16	4.03E18		-656.65	8.73	0.97	5.46	6184.24

5. Conclusions

To address the gap in understanding TR behaviors of LIBs at low-pressure conditions during electrical abuse, this study investigates the impacts of ambient pressure {0.2 atm, 0.6 atm, 1.0 atm} and charging rate {2 C, 3 C, 4 C} on the TR behaviors induced by electrical abuse of commercial 18650-type NCM cells, using an ARC. Furthermore, three stages are defined based on distinct temperature rise rates: Stage I (charging process), Stage II (self-heating period until \$T_{\text{sc}}\$), and Stage III (violent TR phase). Through the analysis of temperature, pressure, voltage, and gas generation characteristics at each stage, the underlying

mechanisms governing the impacts of ambient pressure and charging rate on TR behaviors of NCM cells were investigated. Moreover, the gas generation dynamics models during the TR process were developed. The main conclusions of this study are as follows:

- (1) The safety valve opens earlier in Stage II at lower ambient pressure due to the lower opening pressure of safety valve (\$P_{\text{open}}\$), resulting in a shortened \$\tau_d\$. Furthermore, the reduction in \$\tau_d\$ decreases the electrolyte ejection outside the cell, allowing more electrolyte to remain within the cell and participate in violent TR during Stage III. The additional exotherm leads to increased

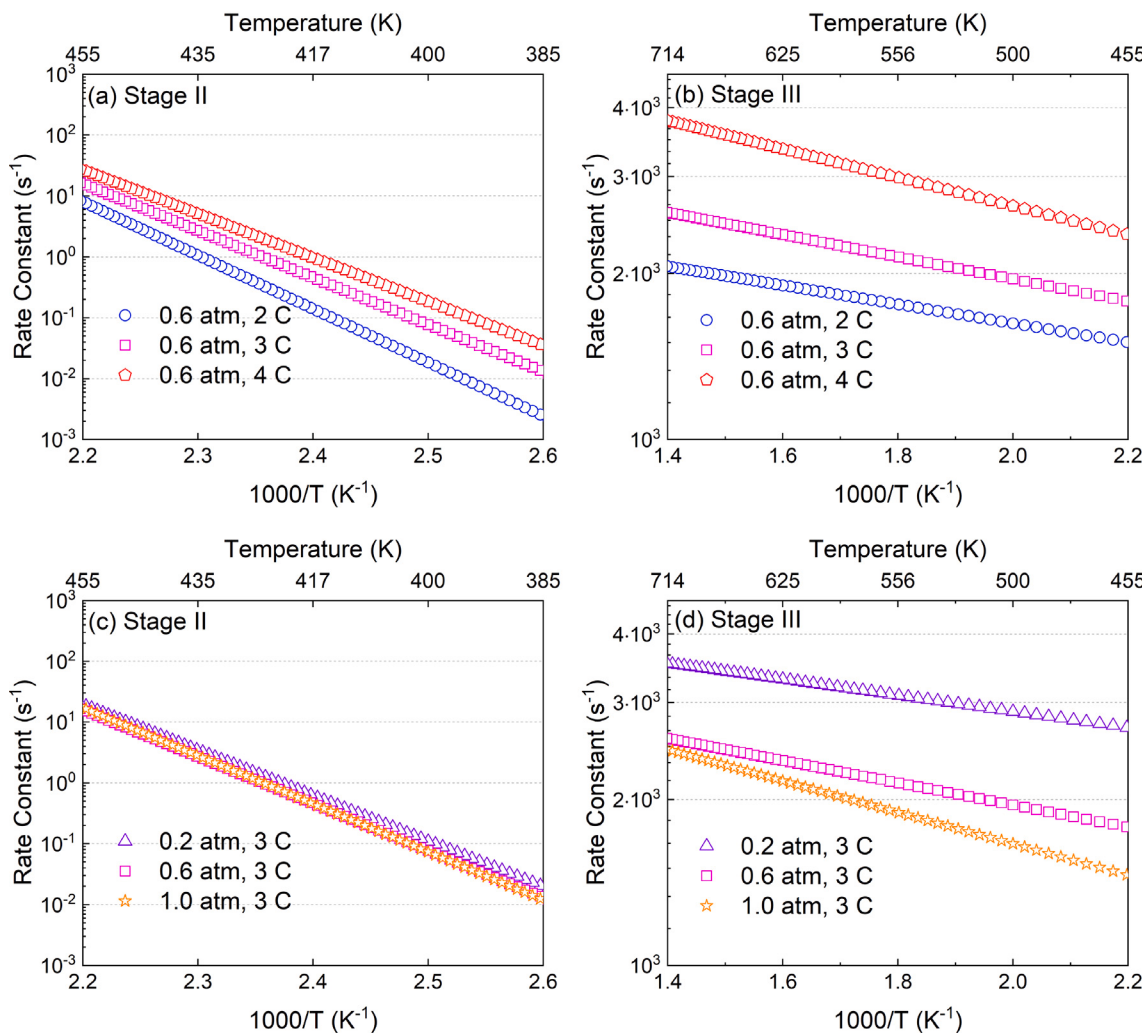


Fig. 9. Comparisons of discovered rate constants for the TR gas generation process with different charging rates {2 C, 3 C, 4 C} in (a) Stage II and (b) Stage III, and different ambient pressures {1.0 atm, 0.6 atm, 0.2 atm} in (c) Stage II and (d) Stage III.

values of T_{max} , P_{max} , and n_{max} , while also reducing T_{sc} . Specifically, T_{sc} decreases from 453.0 K to 448.2 K as ambient pressure decreases from 1.0 atm to 0.2 atm. Additionally, more flammable gases such as CH₄, H₂, and CO are found to be generated at low-pressure conditions, attributed to a more thorough transition of CH₃OH into smaller molecules.

- (2) The increase in charging rate enhances the TR process, primarily due to the greater irreversible heat at higher charging rates. This heightened heat drives the cell into Stage II at a higher temperature, which promotes exothermic side reactions within the cell and increases dT/dt in Stages II and III. Consequently, τ_d is reduced along with higher values of T_{max} , P_{max} , and n_{max} . With the increase in charging rate from 2 C to 4 C, T_{sc} decreases from 466.1 K to 449.0 K. Moreover, a significantly higher proportion of flammable gases, including H₂, CH₄, and CO, is detected at higher charging rates.
- (3) The gas generation dynamics models are developed for TR process. It is observed that both high charging rates and low ambient pressures promote gas generation reactions. However, their effects differ in timing and stages affected: charging rates influence gas generation in both Stages II and III, while ambient pressure primarily affects Stage III after T_{sc} . Additionally, kinetic parameters and rate constants under various ambient pressures and charging rates during Stages II and III are determined. Specifically, the rate constants increase significantly at 0.2 atm compared to those at 1.0 atm, highlighting the increased TR risk

at low-pressure conditions. The construction of gas generation dynamics models contributes to understanding the mechanisms of TR gas generation, while also providing guidance for numerical simulations and prediction models for TR process.

CRediT authorship contribution statement

Shaoyan Liu: Writing – original draft, Methodology, Investigation, Formal analysis, Data curation, Conceptualization. **Qianzhen Guo:** Methodology, Investigation, Data curation. **Jiabo Zhang:** Writing – review & editing, Project administration, Funding acquisition, Conceptualization. **Zhen Huang:** Supervision, Resources, Funding acquisition. **Dong Han:** Writing – review & editing, Supervision, Funding acquisition.

Declaration of competing interest

The authors declare that they have no known competing financial interests or personal relationships that could have appeared to influence the work reported in this paper.

Acknowledgments

This research work is supported by the National Natural Science Foundation of China (Grant No. 52106261) and the Shanghai Pujiang Program (Grant No. 24PJA058).

Data availability

Data will be made available on request.

References

- [1] M. Tariq, A.I. Maswood, C.J. Gajanayake, A.K. Gupta, Aircraft batteries: current trend towards more electric aircraft, *IET Electr. Syst. Transp.* 7 (2) (2017) 93–103, <http://dx.doi.org/10.1049/iet-est.2016.0019>.
- [2] F. Krause, J.-P. Ruiz, S. Jones, E. Brandon, E. Darcy, C. Iannello, R. Bugga, Performance of commercial Li-ion cells for future NASA missions and aerospace applications, *J. Electrochem. Soc.* 168 (4) (2021) 040504, <http://dx.doi.org/10.1149/1945-7111/abf05f>.
- [3] J.A. Mennel, D. Chidambaram, A review on the development of electrolytes for lithium-based batteries for low temperature applications, *Front. Energy* 17 (1) (2023) 43–71, <http://dx.doi.org/10.1007/s11708-022-0853-5>.
- [4] S. Xie, X. Yang, Q. Sun, Z. Wang, Y. He, Research progress and prospects on thermal safety of lithium-ion batteries in aviation low-temperature and low-pressure environments, *J. Energy Storage* 83 (2024) 110734, <http://dx.doi.org/10.1016/j.est.2024.110734>.
- [5] X. Feng, M. Ouyang, X. Liu, L. Lu, Y. Xia, X. He, Thermal runaway mechanism of lithium ion battery for electric vehicles: A review, *Energy Storage Mater.* 10 (2018) 246–267, <http://dx.doi.org/10.1016/j.ensm.2017.05.013>.
- [6] Y.-S. Duh, Y. Sun, X. Lin, J. Zheng, M. Wang, Y. Wang, X. Lin, X. Jiang, Z. Zheng, S. Zheng, G. Yu, Characterization on thermal runaway of commercial 18650 lithium-ion batteries used in electric vehicles: A review, *J. Energy Storage* 41 (2021) 102888, <http://dx.doi.org/10.1016/j.est.2021.102888>.
- [7] Federal Aviation Administration, Events with smoke, fire, extreme heat or explosion involving lithium batteries & lithium battery-powered devices, 2025, https://www.faa.gov/hazmat/resources/lithium_batteries/incidents. (Accessed 22 January 2025).
- [8] United Arab Emirates General Civil Aviation Authority, UPS boeing 747 cargo fire accident: uncontained cargo fire leading to loss of control inflight and uncontrolled descent into terrain, 2010, <https://www.prba.org/wp-content/uploads/2013/07/UAE-Final-Report-UPS-Boeing-747-44AF-N571UP.pdf>.
- [9] N. Williard, W. He, C. Hendricks, M. Pecht, Lessons learned from the 787 dreamliner issue on lithium-ion battery reliability, *Energies* 6 (9) (2013) 4682–4695, <http://dx.doi.org/10.3390/en6094682>.
- [10] S. Cui, Y. Gao, R. Zhu, A new integrated energy system cluster energy sharing framework adapted to high altitude areas, *Appl. Energy* 366 (2024) 123310, <http://dx.doi.org/10.1016/j.apenergy.2024.123310>.
- [11] Power storage facility connects to grid in Xizang, 2024, <https://www.chinadaily.com.cn/a/202411/12/WS67330b68a310f1265a1cce93.html>. (Accessed 15 January 2025).
- [12] China's largest electrochemical storage facility achieves grid connection, 2024, <https://www.ess-news.com/2024/08/19/chinas-largest-electrochemical-storage-facility-achieves-grid-connection/>. (Accessed 15 January 2025).
- [13] World's highest solar plant by elevation goes online in China, 2024, <https://www.pv-magazine.com/2024/12/17/worlds-highest-solar-plant-by-elevation-goes-online-in-china/>. (Accessed 15 January 2025).
- [14] W. Xie, X. Liu, R. He, Y. Li, X. Gao, X. Li, Z. Peng, S. Feng, X. Feng, S. Yang, Challenges and opportunities toward fast-charging of lithium-ion batteries, *J. Energy Storage* 32 (2020) 101837, <http://dx.doi.org/10.1016/j.est.2020.101837>.
- [15] Y. Fu, S. Lu, L. Shi, X. Cheng, H. Zhang, Ignition and combustion characteristics of lithium ion batteries under low atmospheric pressure, *Energy* 161 (2018) 38–45, <http://dx.doi.org/10.1016/j.energy.2018.06.129>.
- [16] Y. Liu, H. Niu, Z. Li, J. Liu, C. Xu, X. Huang, Thermal runaway characteristics and failure criticality of massive ternary li-ion battery piles in low-pressure storage and transport, *Process. Saf. Environ. Prot.* 155 (2021) 486–497, <http://dx.doi.org/10.1016/j.psep.2021.09.031>.
- [17] M. Chen, J. Liu, D. Ouyang, J. Wang, Experimental investigation on the effect of ambient pressure on thermal runaway and fire behaviors of lithium-ion batteries, *Int. J. Energy Res.* 43 (9) (2019) 4898–4911, <http://dx.doi.org/10.1002/er.4666>.
- [18] M. Chen, D. Ouyang, J. Weng, J. Liu, J. Wang, Environmental pressure effects on thermal runaway and fire behaviors of lithium-ion battery with different cathodes and state of charge, *Process. Saf. Environ. Prot.* 130 (2019) 250–256, <http://dx.doi.org/10.1016/j.psep.2019.08.023>.
- [19] S. Xie, L. Ren, X. Yang, H. Wang, Q. Sun, X. Chen, Y. He, Influence of cycling aging and ambient pressure on the thermal safety features of lithium-ion battery, *J. Power Sources* 448 (2020) 227425, <http://dx.doi.org/10.1016/j.jpowsour.2019.227425>.
- [20] G. Zhang, X. Wei, S. Chen, J. Zhu, G. Han, H. Dai, Revealing the impact of slight electrical abuse on the thermal safety characteristics for lithium-ion batteries, *ACS Appl. Energy Mater.* 4 (11) (2021) 12858–12870, <http://dx.doi.org/10.1021/acsaem.1c02537>.
- [21] J. Hu, T. Liu, X. Wang, Z. Wang, L. Wu, Investigation on thermal runaway of 18,650 lithium ion battery under thermal abuse coupled with charging, *J. Energy Storage* 51 (2022) 104482, <http://dx.doi.org/10.1016/j.est.2022.104482>.
- [22] T. Jia, Y. Zhang, C. Ma, S. Li, H. Yu, G. Liu, The early warning for overcharge thermal runaway of lithium-ion batteries based on a composite parameter, *J. Power Sources* 555 (2023) 232393, <http://dx.doi.org/10.1016/j.jpowsour.2022.232393>.
- [23] Z. Huang, J. Liu, H. Zhai, Q. Wang, Experimental investigation on the characteristics of thermal runaway and its propagation of large-format lithium ion batteries under overcharging and overheating conditions, *Energy* 233 (2021) 121103, <http://dx.doi.org/10.1016/j.energy.2021.121103>.
- [24] J. Hu, T. Liu, Q. Tang, X. Wang, Experimental investigation on thermal runaway propagation in the lithium ion battery modules under charging condition, *Appl. Therm. Eng.* 211 (2022) 118522, <http://dx.doi.org/10.1016/j.aplthermaleng.2022.118522>.
- [25] L. Oca, N. Guillet, R. Tessard, U. Iraola, Lithium-ion capacitor safety assessment under electrical abuse tests based on ultrasound characterization and cell opening, *J. Energy Storage* 23 (2019) 29–36, <http://dx.doi.org/10.1016/j.est.2019.02.033>.
- [26] Y. Qiu, F. Jiang, A review on passive and active strategies of enhancing the safety of lithium-ion batteries, *Int. J. Heat Mass Transfer* 184 (2022) 122288, <http://dx.doi.org/10.1016/j.ijheatmasstransfer.2021.122288>.
- [27] D. Belov, M.-H. Yang, Failure mechanism of li-ion battery at overcharge conditions, *J. Solid State Electrochem.* 12 (2008) 885–894, <http://dx.doi.org/10.1007/s10008-007-0449-3>.
- [28] G. Zeng, Z. Bai, P. Huang, Q. Wang, Thermal safety study of li-ion batteries under limited overcharge abuse based on coupled electrochemical-thermal model, *Int. J. Energy Res.* 44 (5) (2020) 3607–3625, <http://dx.doi.org/10.1002/er.5125>.
- [29] L. Wu, K.-W. Nam, X. Wang, Y. Zhou, J.-C. Zheng, X.-Q. Yang, Y. Zhu, Structural origin of overcharge-induced thermal instability of Ni-containing layered-cathodes for high-energy-density lithium batteries, *Chem. Mater.* 23 (17) (2011) 3953–3960, <http://dx.doi.org/10.1021/cm201452q>.
- [30] T. Waldmann, B.-I. Hogg, M. Wohlfahrt-Mehrens, Li plating as unwanted side reaction in commercial Li-ion cells – a review, *J. Power Sources* 384 (2018) 107–124, <http://dx.doi.org/10.1016/j.jpowsour.2018.02.063>.
- [31] S. Xie, J. Sun, X. Chen, Y. He, Thermal runaway behavior of lithium-ion batteries in different charging states under low pressure, *Int. J. Energy Res.* 45 (4) (2021) 5795–5805, <http://dx.doi.org/10.1002/er.6200>.
- [32] C. Ding, N. Zhu, J. Yu, Y. Li, X. Sun, C. Liu, Q. Huang, J. Wang, Experimental investigation of environmental pressure effects on thermal runaway properties of 21700 lithium-ion batteries with high energy density, *Case Stud. Therm. Eng.* 38 (2022) 102349, <http://dx.doi.org/10.1016/j.csite.2022.102349>.
- [33] Q. Sun, H. Liu, M. Zhi, X. Chen, P. Lv, Y. He, Thermal characteristics of thermal runaway for pouch lithium-ion battery with different state of charges under various ambient pressures, *J. Power Sources* 527 (2022) 231175, <http://dx.doi.org/10.1016/j.jpowsour.2022.231175>.
- [34] P.J. Bugryniec, E.G. Resendiz, S.M. Nwophoke, S. Khanna, C. James, S.F. Brown, Review of gas emissions from lithium-ion battery thermal runaway failure—Considering toxic and flammable compounds, *J. Energy Storage* 87 (2024) 111288, <http://dx.doi.org/10.1016/j.est.2024.111288>.
- [35] Z. Jia, P. Qin, Z. Li, Z. Wei, K. Jin, L. Jiang, Q. Wang, Analysis of gas release during the process of thermal runaway of lithium-ion batteries with three different cathode materials, *J. Energy Storage* 50 (2022) 104302, <http://dx.doi.org/10.1016/j.est.2022.104302>.
- [36] J. Zhang, Q. Guo, S. Liu, C. Zhou, Z. Huang, D. Han, Investigation on gas generation and corresponding explosion characteristics of lithium-ion batteries during thermal runaway at different charge states, *J. Energy Storage* 80 (2024) 110201, <http://dx.doi.org/10.1016/j.est.2023.110201>.
- [37] D. Ren, X. Liu, X. Feng, L. Lu, M. Ouyang, J. Li, X. He, Model-based thermal runaway prediction of lithium-ion batteries from kinetics analysis of cell components, *Appl. Energy* 228 (2018) 633–644, <http://dx.doi.org/10.1016/j.apenergy.2018.06.126>.
- [38] Y. He, L. Zhang, D. Zhang, Z. Wang, Y. Liu, Experimental and computational analyses of thermal runaway behavior of lithium ion pouch battery at low ambient pressure, *J. Electrochem. Energy Convers. Storage* 20 (4) (2023) 041007, <http://dx.doi.org/10.1115/1.4056328>.
- [39] B. Mao, C. Fear, H. Chen, H. Zhou, C. Zhao, P.P. Mukherjee, J. Sun, Q. Wang, Experimental and modeling investigation on the gas generation dynamics of lithium-ion batteries during thermal runaway, *ETransportation* 15 (2023) 100212, <http://dx.doi.org/10.1016/j.etran.2022.100212>.
- [40] D. Ren, H. Hsu, R. Li, X. Feng, D. Guo, X. Han, L. Lu, X. He, S. Gao, J. Hou, et al., A comparative investigation of aging effects on thermal runaway behavior of lithium-ion batteries, *ETransportation* 2 (2019) 100034, <http://dx.doi.org/10.1016/j.etran.2019.100034>.
- [41] G. Zhang, X. Wei, X. Wang, S. Chen, J. Zhu, H. Dai, Evolution mechanism and non-destructive assessment of thermal safety for lithium-ion batteries during the whole lifecycle, *Nano Energy* 126 (2024) 109621, <http://dx.doi.org/10.1016/j.nanoen.2024.109621>.
- [42] L. Zhang, L. Liu, A. Terekhov, D. Warnberg, P. Zhao, Thermal runaway of Li-ion battery with different aging histories, *Process. Saf. Environ. Prot.* 185 (2024) 910–917, <http://dx.doi.org/10.1016/j.psep.2024.03.077>.

- [43] G. Zhang, X. Wei, D. Chen, X. Wang, S. Chen, J. Zhu, H. Dai, Thermal characteristic evolution of lithium-ion batteries during the whole lifecycle, *J. Energy Chem.* 92 (2024) 534–547, <http://dx.doi.org/10.1016/j.jecchem.2024.01.036>.
- [44] Q. Guo, S. Liu, J. Zhang, Z. Huang, D. Han, Effects of charging rates on heat and gas generation in lithium-ion battery thermal runaway triggered by high temperature coupled with overcharge, *J. Power Sources* 600 (2024) 234237, <http://dx.doi.org/10.1016/j.jpowsour.2024.234237>.
- [45] S. Humphreys, R. Deyermond, I. Bali, M. Stevenson, J. Fee, The effect of high altitude commercial air travel on oxygen saturation, *Anaesthesia* 60 (5) (2005) 458–460, <http://dx.doi.org/10.1111/j.1365-2044.2005.04124.x>.
- [46] M. Chen, J. Liu, Y. He, R. Yuan, J. Wang, Study of the fire hazards of lithium-ion batteries at different pressures, *Appl. Therm. Eng.* 125 (2017) 1061–1074, <http://dx.doi.org/10.1016/j.applthermaleng.2017.06.131>.
- [47] L. Lu, X. Han, J. Li, J. Huia, M. Ouyang, A review on the key issues for lithium-ion battery management in electric vehicles, *J. Power Sources* 226 (2013) 272–288, <http://dx.doi.org/10.1016/j.jpowsour.2012.10.060>.
- [48] X. Feng, M. Fang, X. He, M. Ouyang, L. Lu, H. Wang, M. Zhang, Thermal runaway features of large format prismatic lithium ion battery using extended volume accelerating rate calorimetry, *J. Power Sources* 255 (2014) 294–301, <http://dx.doi.org/10.1016/j.jpowsour.2014.01.005>.
- [49] P. Qin, J. Sun, Q. Wang, A new method to explore thermal and venting behavior of lithium-ion battery thermal runaway, *J. Power Sources* 486 (2021) 229357, <http://dx.doi.org/10.1016/j.jpowsour.2020.229357>.
- [50] X. Liu, D. Ren, H. Hsu, X. Feng, G.-L. Xu, M. Zhuang, H. Gao, L. Lu, X. Han, Z. Chu, et al., Thermal runaway of lithium-ion batteries without internal short circuit, *Joule* 2 (10) (2018) 2047–2064, <http://dx.doi.org/10.1016/j.joule.2018.06.015>.
- [51] B. Ma, J. Liu, R. Yu, Study on the flammability limits of lithium-ion battery vent gas under different initial conditions, *ACS Omega* 5 (43) (2020) 28096–28107, <http://dx.doi.org/10.1021/acsomega.0c03713>.
- [52] R. Yu, J. Liu, W. Liang, C.K. Law, H. Wang, M. Ouyang, On explosion limits of NCA battery vent gas, *Proc. Combust. Inst.* 39 (3) (2023) 3031–3040, <http://dx.doi.org/10.1016/j.proci.2022.11.010>.
- [53] R. Yu, J. Liu, W. Liang, C.K. Law, H. Wang, M. Ouyang, On flammability limits of battery vent gas: Role of diffusion, radiation and chemical kinetics, *Cambust. Flame* 249 (2023) 112631, <http://dx.doi.org/10.1016/j.combustflame.2023.112631>.
- [54] J.K. Ostanek, W. Li, P.P. Mukherjee, K. Crompton, C. Hacker, Simulating onset and evolution of thermal runaway in Li-ion cells using a coupled thermal and venting model, *Appl. Energy* 268 (2020) 114972, <http://dx.doi.org/10.1016/j.apenergy.2020.114972>.
- [55] S. Hoelle, S. Scharner, S. Asanin, O. Hinrichsen, Analysis on thermal runaway behavior of prismatic lithium-ion batteries with autoclave calorimetry, *J. Electrochem. Soc.* 168 (12) (2021) 120515, <http://dx.doi.org/10.1149/1945-7111/ac3c27>.
- [56] P.T. Coman, S. Mátéfi-Tempfli, C.T. Veje, R.E. White, Modeling vaporization, gas generation and venting in Li-ion battery cells with a dimethyl carbonate electrolyte, *J. Electrochem. Soc.* 164 (9) (2017) A1858, <http://dx.doi.org/10.1149/2.0631709jes>.
- [57] H. Yang, H. Bang, K. Amine, J. Prakash, Investigations of the exothermic reactions of natural graphite anode for li-ion batteries during thermal runaway, *J. Electrochem. Soc.* 152 (1) (2004) A73, <http://dx.doi.org/10.1149/1.1836126>.
- [58] J.-i. Yamaki, H. Takatsuji, T. Kawamura, M. Egashira, Thermal stability of graphite anode with electrolyte in lithium-ion cells, *Solid State Ion.* 148 (3–4) (2002) 241–245, [http://dx.doi.org/10.1016/S0167-2738\(02\)00060-7](http://dx.doi.org/10.1016/S0167-2738(02)00060-7).
- [59] H. Wang, A. Tang, K. Huang, Oxygen evolution in overcharged $\text{Li}_{\text{x}}\text{Ni}_{1/3}\text{Co}_{1/3}\text{Mn}_{1/3}\text{O}_2$ electrode and its thermal analysis kinetics, *Chin. J. Chem.* 29 (8) (2011) 1583–1588, <http://dx.doi.org/10.1002/cjoc.201108284>.
- [60] Q. Zhang, T. Liu, C. Hao, Y. Qu, J. Niu, Q. Wang, D. Chen, In situ Raman investigation on gas components and explosion risk of thermal runaway emission from lithium-ion battery, *J. Energy Storage* 56 (2022) 105905, <http://dx.doi.org/10.1016/j.est.2022.105905>.
- [61] S. Hess, M. Wohlfahrt-Mehrens, M. Wachtler, Flammability of li-ion battery electrolytes: flash point and self-extinguishing time measurements, *J. Electrochem. Soc.* 162 (2) (2015) A3084, <http://dx.doi.org/10.1149/2.0121502jes>.
- [62] X. Feng, S. Zheng, D. Ren, X. He, L. Wang, H. Cui, X. Liu, C. Jin, F. Zhang, C. Xu, et al., Investigating the thermal runaway mechanisms of lithium-ion batteries based on thermal analysis database, *Appl. Energy* 246 (2019) 53–64, <http://dx.doi.org/10.1016/j.apenergy.2019.04.009>.
- [63] Q. Wang, L. Jiang, Y. Yu, J. Sun, Progress of enhancing the safety of lithium ion battery from the electrolyte aspect, *Nano Energy* 55 (2019) 93–114, <http://dx.doi.org/10.1016/j.nanoen.2018.10.035>.
- [64] B. Mao, P. Huang, H. Chen, Q. Wang, J. Sun, Self-heating reaction and thermal runaway criticality of the lithium ion battery, *Int. J. Heat Mass Transfer* 149 (2020) 119178, <http://dx.doi.org/10.1016/j.ijheatmasstransfer.2019.119178>.
- [65] J.-S. Shin, C.-H. Han, U.-H. Jung, S.-I. Lee, H.-J. Kim, K. Kim, Effect of Li_2CO_3 additive on gas generation in lithium-ion batteries, *J. Power Sources* 109 (1) (2002) 47–52, [http://dx.doi.org/10.1016/S0378-7753\(02\)00039-3](http://dx.doi.org/10.1016/S0378-7753(02)00039-3).
- [66] K.C. Abbott, J.E. Buston, J. Gill, S.L. Goddard, D. Howard, G. Howard, E. Read, R.C. Williams, Comprehensive gas analysis of a 21700 $\text{Li}(\text{Ni}_{0.8}\text{Co}_{0.1}\text{Mn}_{0.1})\text{O}_2$ cell using mass spectrometry, *J. Power Sources* 539 (2022) 231585, <http://dx.doi.org/10.1016/j.jpowsour.2022.231585>.
- [67] J. Zhang, A. Zhong, Z. Huang, D. Han, Experimental and kinetic study on the stabilities and gas generation of typical electrolyte solvent components under oxygen-lean oxidation and pyrolysis conditions, *Sci. China Technol. Sci.* 65 (12) (2022) 2883–2894, <http://dx.doi.org/10.1007/s11431-022-2184-x>.
- [68] K. Onda, T. Ohshima, M. Nakayama, K. Fukuda, T. Araki, Thermal behavior of small lithium-ion battery during rapid charge and discharge cycles, *J. Power Sources* 158 (1) (2006) 535–542, <http://dx.doi.org/10.1016/j.jpowsour.2005.08.049>.
- [69] P.T. Coman, S. Rayman, R.E. White, A lumped model of venting during thermal runaway in a cylindrical lithium cobalt oxide lithium-ion cell, *J. Power Sources* 307 (2016) 56–62, <http://dx.doi.org/10.1016/j.jpowsour.2015.12.088>.
- [70] A.W. Golubkov, S. Scheikl, R. Planteu, G. Voitic, H. Wiltsche, C. Stangl, G. Fauler, A. Thaler, V. Hacker, Thermal runaway of commercial 18650 Li-ion batteries with LFP and NCA cathodes—impact of state of charge and overcharge, *Rsc Adv.* 5 (70) (2015) 57171–57186, <http://dx.doi.org/10.1039/C5RA05897>.
- [71] S. Koch, A. Fill, K.P. Birke, Comprehensive gas analysis on large scale automotive lithium-ion cells in thermal runaway, *J. Power Sources* 398 (2018) 106–112, <http://dx.doi.org/10.1016/j.jpowsour.2018.07.051>.
- [72] P. Huang, P. Ping, K. Li, H. Chen, Q. Wang, J. Wen, J. Sun, Experimental and modeling analysis of thermal runaway propagation over the large format energy storage battery module with $\text{Li}_4\text{Ti}_5\text{O}_{12}$ anode, *Appl. Energy* 183 (2016) 659–673, <http://dx.doi.org/10.1016/j.apenergy.2016.08.160>.
- [73] J. Sun, Z. Sun, Q. Wang, H. Ding, T. Wang, C. Jiang, Catalytic effects of inorganic acids on the decomposition of ammonium nitrate, *J. Hazard. Mater.* 127 (1–3) (2005) 204–210, <http://dx.doi.org/10.1016/j.jhazmat.2005.07.028>.
- [74] J. Schmitt, B. Kraft, J.P. Schmidt, B. Meir, K. Elian, D. Ensling, G. Keser, A. Jossen, Measurement of gas pressure inside large-format prismatic lithium-ion cells during operation and cycle aging, *J. Power Sources* 478 (2020) 228661, <http://dx.doi.org/10.1016/j.jpowsour.2020.228661>.
- [75] X. Feng, X. He, M. Ouyang, L. Lu, P. Wu, C. Kulp, S. Prasser, Thermal runaway propagation model for designing a safer battery pack with 25 Ah $\text{LiNi}_{x}\text{Co}_y\text{Mn}_{z}\text{O}_2$ = large format lithium ion battery, *Appl. Energy* 154 (2015) 74–91, <http://dx.doi.org/10.1016/j.apenergy.2015.04.118>.
- [76] B. Mao, H. Chen, Z. Cui, T. Wu, Q. Wang, Failure mechanism of the lithium ion battery during nail penetration, *Int. J. Heat Mass Transfer* 122 (2018) 1103–1115, <http://dx.doi.org/10.1016/j.ijheatmasstransfer.2018.02.036>.
- [77] D. Kong, G. Wang, P. Ping, J. Wen, A coupled conjugate heat transfer and CFD model for the thermal runaway evolution and jet fire of 18650 lithium-ion battery under thermal abuse, *Etransportation* 12 (2022) 100157, <http://dx.doi.org/10.1016/j.etrans.2022.100157>.
- [78] C. He, Q. Yue, Q. Chen, T. Zhao, Modeling thermal runaway of lithium-ion batteries with a venting process, *Appl. Energy* 327 (2022) 120110, <http://dx.doi.org/10.1016/j.apenergy.2022.120110>.
- [79] Z. Cheng, Y. Min, P. Qin, Y. Zhang, J. Li, W. Mei, Q. Wang, A distributed thermal-pressure coupling model of large-format lithium iron phosphate battery thermal runaway, *Appl. Energy* 378 (2025) 124875, <http://dx.doi.org/10.1016/j.apenergy.2024.124875>.
- [80] X.-X. Wang, Q.-T. Li, X.-Y. Zhou, Y.-M. Hu, X. Guo, Monitoring thermal runaway of lithium-ion batteries by means of gas sensors, *Sensors Actuators B: Chem.* (2024) 135703, <http://dx.doi.org/10.1016/j.snb.2024.135703>.
- [81] D. Hu, S. Huang, Z. Wen, X. Gu, J. Lu, A review on thermal runaway warning technology for lithium-ion batteries, *Renew. Sustain. Energy Rev.* 206 (2024) 114882, <http://dx.doi.org/10.1016/j.rser.2024.114882>.